Entropic control of HD exchange rates over dilute Pd-in-Au alloy nanoparticle catalysts

Jessi E.S. van der Hoeven[1,2], Hio Tong Ngan[3], Austin Taylor[1], Nathaniel M. Eagan[1], Joanna Aizenberg[1,2], Philippe Sautet[3,4], Robert J. Madix[2] and Cynthia M. Friend[1,2*]

[1]*Department of Chemistry and Chemical Biology, Harvard University, Cambridge, MA 02138, USA*

[2]*Harvard John A. Paulson School of Engineering and Applied Sciences, Harvard University, Cambridge, MA 02138, USA*

[3]*Department of Chemical and Biomolecular Engineering, University of California, Los Angeles, California 90095, United States*

[4]*Department of Chemistry and Biochemistry, University of California, Los Angeles, California 90095, United States*

*E-mail: friend@fas.harvard.edu

Abstract

Dilute Pd-in-Au alloy catalysts are promising materials for selective hydrogenation catalysis. Extensive surface science studies have contributed mechanistic insight on the energetic aspect of hydrogen dissociation, migration and recombination on dilute alloy systems. Yet, translating these fundamental concepts to the kinetics and free energy of hydrogen dissociation on nanoparticle catalysts operating at ambient pressures and temperatures remains challenging. Here, the effect of the Pd concentration and Pd ensemble size on the catalytic activity, apparent activation energy and rate limiting process is addressed by combining experiment and theory. Experiments in a flow reactor show that a compositional change from 4 to 8 atm% Pd of the Pd-in-Au alloy catalyst leads to strong increase in activity, even exceeding the activity per Pd atom of monometallic Pd under the same conditions, albeit with an increase in apparent activation energy. First-principles calculations show that the rate and apparent activation enthalpy for HD exchange increase when increasing the Pd ensemble size from single Pd atoms to Pd trimers in a Au surface, suggesting that the ensemble size distribution shifts from mainly single Pd atoms on the 4 atm% Pd alloy to larger Pd ensembles of at least three atoms for the 8 atm% Pd/Au catalyst. The DFT studies also indicated that the rate-controlling process is different: H_2 (D_2) dissociation determines the rate for single atoms whereas recombination of adsorbed H and D determines the rate on Pd trimers, similar to bulk Pd.

Both experiment and theory suggest that the increased reaction rate with increasing Pd content and ensemble size stems from an entropic driving force. Finally, our results support hydrogen migration between Pd sites via Au and indicate that the dilute alloy design prevents the formation of subsurface hydrogen, which is crucial in achieving high selectivity in hydrogenation catalysis.

Key words: catalysis, bimetallic, dilute alloy, hydrogen dissociation, density-functional theory, palladium, gold

Introduction

A key challenge in the hydrogenation of polyunsaturated hydrocarbons is the design of materials with both a high chemoselectivity and sufficiently high catalytic activity.[1–3] Dilute alloys are a promising class of materials for addressing this challenge, in particular the combination of a selective coinage metal host (Au, Ag, Cu) and a small amount of a more active metal dopant such as Pd.[4–9] Optimization of dilute alloys for selective hydrogenation relies on carefully tuning the dopant concentration, since high dopant concentrations typically lead to higher hydrogenation activities but lower selectivity.[6–8] Conversely, decreasing the Pd concentration can substantially increase the selectivity, but will lower the catalytic activity. However, the activity per Pd surface atom can deviate from these general trends, and in certain cases even exceed that of Pd atoms in pure Pd.[6] A general understanding of such compositional effects requires insight in the catalyst's ability to dissociate hydrogen, which is a key step for hydrogenation catalysis. Yet, relating the hydrogenation performance of dilute alloys to their intrinsic hydrogen dissociation activity is often complicated by the presence of more strongly binding reactants. For instance, alkynes and dienes can block hydrogen dissociation sites,[5] induce hydrogen migration[5,10] and even alter the surface structure of the catalyst by preferentially segregating the Pd atoms to the surface.[11]

A powerful model reaction for disentangling the catalyst's intrinsic hydrogen dissociation activity from such restructuring and co-adsorption effects is HD exchange ($H_2 + D_2 \rightarrow 2HD$). HD exchange has been previously studied over dilute alloy systems in a surface science context and on well-defined alloy surfaces.[12,13] Dissociation of H_2 and the reverse reaction, H atom recombination, typically occur on the Pd-sites, due to the high barrier on Au.[10] The hydrogen atom binding strength depends on the Pd ensemble size, being relatively weak on single Pd atoms and somewhat stronger on larger clusters.[12,14] However these surface science studies provide contrasted conclusions on the minimum Pd_n ensemble required for H_2 dissociation (from 1 to 4) and the knowledge on the influence of the surface alloy ensembles on the kinetics of the H_2 dissociation and HD exchange remains limited. Whether hydrogen migration from Pd

onto the host metals like Au, Ag, and Cu occurs is also a matter of debate, as these metals bind hydrogen more weakly. Yet, spill-over from Pd has been reported for Au-Pd,[5,10,12] Ag-Pd[15] and Cu-Pd[16] alloys at sufficiently high hydrogen pressure and coverage.[15]

Despite extensive work from the surface science community on hydrogen dissociation and migration behavior on dilute alloys, these concepts have yet to be extended to nanoparticle catalysts operating at pressures and temperatures relevant for catalytic applications. Here, we achieve this by measuring the intrinsic hydrogen dissociation activity of dilute Pd-in-Au nanoparticle (NP) catalysts at moderate pressures in a flow reactor using the HD exchange reaction. A combined catalysis and density functional theory approach showed how the Pd concentration and ensemble size at the surface impact activity and apparent activation energy of hydrogen dissociation and recombination on dilute alloy catalysts. We specifically show that the nature of the Pd ensemble controls the free energy profile of the H_2 dissociation and recombination reaction, and the nature of the kinetically controlling intermediate and transition state (TS), with a main role of entropic effects.

Results

Preparation of the dilute alloy nanoparticle catalysts

The dilute Pd-in-Au alloy catalysts were prepared using the raspberry colloid templated (RCT) approach, a multistep colloidal synthesis route yielding well-defined macroporous metal-oxide supports with nanoparticles partially embedded in the pore walls.[17–19] The partial nanoparticle embedding prevents sintering of the nanoparticles in the RCT catalysts at elevated temperatures and under reaction conditions.[18,20] Two dilute Pd in Au catalysts were prepared, one with 4 atm% Pd and one with 8 atm% Pd. These will be referred to as to as Pd_4Au_{96} and Pd_8Au_{92} respectively. As we aimed to study the catalytic behavior of the metal nanoparticles, silica was chosen as the supporting oxide, which is known to be relatively inert and non-reducible. The monometallic counterparts, Pd_0Au_{100} and $Pd_{100}Au_0$, and pure SiO_2 RCT catalysts containing no NPs were prepared for comparison. The full set of synthesis details is provided in the Methods section. Table 1 summarizes the key structural parameters for all samples as obtained from transmission electron microscopy (TEM) and inductively coupled plasma mass spectrometry (ICP-MS) analysis, and the amount of catalyst that was loaded to the reactor.

The well-defined structural properties of the bimetallic RCT catalyst are evident from the electron microscopy images (Figure 1). The ordered pore structure of the silica support, where the macropores had an average pore diameter of 295 nm, is evident from the SEM image (Figure 1a). Within the silica pore

walls 4.9±0.9 nm Pd_4Au_{96} NPs were embedded as shown in the bright field transmission electron microscopy image in Figure 1b. Higher resolution HAADF-STEM imaging revealed that the particles had a decahedral, penta-twinned crystal structure with {111} Face-Centered Cubic (FCC) crystal facets at the particle surface (Figure 1c), which is in line with more detailed 3D characterization work by our group[18] and commonly observed for gold nanoparticles synthesized using citrate ligands.[21–23] Elemental dispersive X-ray spectroscopy (EDS) maps (Figures 1d, Figure S1) indicate homogeneous mixing of Pd and Au in the nanoparticles after pretreatment in 20% O_2 at 500 °C. The similarly shaped intensity profiles for Pd and Au (Figure 1e) confirm the metal distribution is likely a random alloy. Note that EDS is not sufficiently sensitive to determine the exact surface composition or the size of the Pd ensembles at the nanoparticle surface.

Catalytic performance of the bimetallic Au-Pd catalyst in the HD exchange reaction

Apparent activation energies for the HD exchange reaction were measured over the dilute alloy Pd_4Au_{96} and Pd_8Au_{92} catalysts with flow reactor measurements at varying temperatures. Prior to the reaction the catalysts were activated by segregating Pd to the surface in a 20% O_2 in Ar mixture at 773 K.[6,24,25] The exchange reaction was carried out in 10% H_2 10% D_2 in Ar following a stepwise temperature profile, which ensured steady state conditions at fixed temperatures. To verify whether irreversible structural changes occurred during the reaction, the catalytic activity was probed during cycles of heating and cooling. Mass spectrometry (MS) was employed to monitor the reaction rate and to quantify the product formation. A detailed description of the quantitative MS analysis can be found in the Methods.

The extent of H-D exchange catalyzed by Pd_4Au_{96} RCT SiO_2 under flow depends on the reaction temperature (Figure 2a). The HD signal increased with increasing temperature, whereas the H_2 and D_2 signals decreased. The conversion to HD increased from 0 to 26% between 303 to 473 K; the maximum possible conversion is 50%, corresponding to a statistical mixture of $1H_2$:$1D_2$:2HD (indicated by "equilibrium composition"). The activity-vs-temperature curves for HD exchange catalyzed by the Pd_4Au_{96} RCT SiO_2 are nearly superimposable for heating and cooling, indicating that no irreversible structural changes occurred upon heating.

The dependence of the conversion on temperature was used to extract the apparent activation energies for HD exchange through construction of Arrhenius plots (Figure 2c). Only the average rates from the isothermal steps were included in the Arrhenius plot as these were obtained under steady state conditions. Furthermore, only the data between 1 and 20% conversion were included in the analysis because the contribution of the reverse reaction becomes significant at higher conversion, leading to seemingly lower apparent activation energies. Conversion data below 1% were also excluded, because slight deviations in

the base line correction can induce significant errors in the calculated rate. The Arrhenius plots yielded an apparent activation energy of 0.33±0.04 eV (32±3.8 kJ/mole) and an intercept $Ln(HD\ exchange\ rate)_{\frac{1}{T}=0}$ of 17±1.2. From the intercept the apparent pre-exponential factor was calculated to be $2.1 \cdot 10^{8}$ $\mu mol_{HD}\ s^{-1}\ g_{metal}^{-1}$ using the rate order from Figure S2 (see Methods for details).

The apparent activation energy and pre-exponential factor depend strongly on the Pd content in the Pd-in-Au nanoparticles, as illustrated by the measurement of HD exchange rates over the Pd_8Au_{92} RCT SiO_2 catalyst (Figure 3, Table 2). Furthermore, at this higher Pd content, the conversion exhibits a hysteresis when the temperatures are changed using heating vs cooling. Specifically, the apparent activation energies obtained from heating and cooling were 0.71 ±0.04 eV and 0.59±0.07 eV, respectively. The pre-exponential factor also changed from $1.2 \cdot 10^{14}$ $\mu mol_{HD}\ s^{-1}\ g_{metal}^{-1}$ when heating to $3.1 \cdot 10^{12}$ $\mu mol_{HD}\ s^{-1}\ g_{metal}^{-1}$ when cooling the Pd_8Au_{92} RCT SiO_2 catalyst (Figure 3b), indicating that some structural changes might have occurred. Indeed, the Pd_8Au_{92} sample deactivated above 403 K, possibly due to surface restructuring by Pd dissolution into the bulk, while the Pd_4Au_{96} sample was much more thermally stable, with consistent behavior up to 473 K.

To investigate the H and D surface coverage of the dilute alloy during HD exchange, reaction order experiments were performed at steady state and relatively low conversion (5% HD conversion) (Figure S2). In the first set of such experiments the H_2+D_2 pressure was varied where pH_2=pD_2 (Figure 2a); in the second set the D_2 pressure was varied while keeping pH_2>>pD_2 (Figure 2b). In both cases a first order relation between the rate of HD formation and the $p(D_2)$ pressure was measured for Pd_4Au_{96} and Pd_8Au_{92}. This result indicates that Pd sites in the Pd_4Au_{96} and Pd_8Au_{92} catalysts were not saturated with H and D, as saturation of the Pd sites would result in zero order behavior. Analogous reaction order experiments performed on monometallic Pd RCT SiO_2 yielded slightly lower reaction orders of 0.71 and 0.89 in the D_2 partial pressure for conditions where pH_2=pD_2 and pH_2>>pD_2, respectively, indicating a higher surface coverage compared to the bimetallic catalysts.

The Pd_4Au_{96} catalyst was stable up to 473 K under reaction conditions (10% H_2, 10% D_2), whereas the Pd_8Au_{92} catalyst already deactivated below 403 K. Their activity was readily recovered by repeating the oxidative pretreatment at 773 K. The deactivation is attributed to dissolution of Pd surface clusters and Pd migration to the subsurface at higher temperatures, which can be reversed by pretreatment in oxygen as reported in previous work.[24]

Comparing the bimetallic catalysts to their monometallic counterparts

Interestingly, the Pd_8Au_{92} RCT SiO_2 sample was more active per accessible Pd atom than pure Pd RCT SiO_2 (Figure 4). The trend in measured activity is $Pd_8Au_{92} > Pd_{100}Au_0 > Pd_4Au_{96} >> Pd_0Au_{100}$, based on the turnover frequency (TOF), expressed in number of HD molecules converted per second per Pd surface atom for Pd_4Au_{96}, Pd_8Au_{92} and $Pd_{100}Au_0$, and per Au surface atom for Pd_0Au_{100}. In calculating the TOF, the following assumptions were made regarding the nanoparticle particle shape, size and surface composition based on the TEM results (Figure 1 and Table 1): i) the particles had decahedral particle shape with {111} FCC surface facets, ii) the average particle sizes were 4.9 (Pd_4Au_{96}), 5.6 (Pd_8Au_{92}) and 6.9 nm ($Pd_{100}Au_0$ and Pd_0Au_{100}), iii) the Pd surface composition was the same as the bulk metal composition, and iv) the nanoparticle surface is fully accessible, although the accessibility is likely lower due to the partial embedding of the nanoparticles in the RCT catalysts[18] The catalytic activity was normalized by the number of Pd surface atoms, as they are likely the active site in the bimetallic catalysts. This is further supported by the very low activity of pure Pd_0Au_{100}, which is more than 2 orders of magnitude smaller than that of the bimetallic catalysts. The HD exchange rate per gram of metal loaded to the reactor (Figure S3a) and per gram of Pd (Figure S3b) are provided in the SI and also include the activity of the bare silica support.

There are also substantial differences in apparent activation energy and pre-exponential factor among the catalysts (Table 2). The apparent activation energies decreased in order of $Pd_8Au_{92} > Pd_{100}Au_0 > Pd_4Au_{96}$. The values for Pd_0Au_{100} are not reported as this sample showed negligible activity in the temperature range in which the apparent activation energies were calculated for the other catalysts. The corresponding conversion and Arrhenius plots for $Pd_{100}Au_0$ are provided in Figure S4. In addition to a clear difference in apparent activation energy, a substantial difference in the pre-exponential factor was observed. The pre-exponential of $Pd_8Au_{92} > Pd_{100}Au_0 > Pd_4Au_{96}$; the pre-exponential factor of Pd_8Au_{92} was $6 \cdot 10^5$ times larger than that of Pd_4Au_{96}.

There is significant hysteresis between heating and cooling for the $Pd_{100}Au_0$ RCT SiO_2 catalysts (Figure S4). The increase in activity upon cooling stems from an increase in pre-exponential factor. The hysteresis was reproducible upon cycling the catalyst for multiple heating and cooling cycles, indicating that it is due to a reversible process. Additionally, the hysteresis is dependent on the maximum temperature used in the experiments, where heating to higher temperatures led to larger differences in activity between heating and cooling. The hysteresis for the pure Pd catalysts was most likely due to reversible hydride formation,[26] which is known to alter hydrogen dissociation behavior.[27] No strong hysteresis and increase in pre-

exponential factor was observed upon cooling for the dilute alloys (Figure 2 and 3), confirming that no subsurface hydride was formed in the dilute alloy catalysts during HD exchange.

Summarizing, the experiments show a large influence of the Pd content of dilute Pd-in-Au alloys on the kinetics of HD exchange, with a larger activity but also a higher activation enthalpy barrier for Pd_8Au_{92} compared to Pd_4Au_{96}. The increased activity is therefore not controlled by the reaction enthalpy but by the reaction entropy, as illustrated by the strong change in pre-exponential factor, with an increase by more than 5 orders of magnitude for Pd_8Au_{92} compared to $Pd_4Au_{96.}$ We will show now, from first principle calculations, that these changes can be explained by the presence of different ensembles of Pd atoms at the surface of these two alloys.

Ensemble size effect on hydrogen dissociation, migration and recombination barriers

DFT calculations clearly show that there is a strong effect of the Pd ensemble size on the reaction pathway and effective barrier for hydrogen dissociation, migration, and recombination on dilute alloy surfaces (Figure 5, Figure S5). Thermal and zero-point energy effects are fully included in the calculated enthalpy and entropy, therefore differentiating H and D from their masses. Intermediates and transition states from D_2 are slightly less stable (by up to 0.05 eV). Three models were investigated: single Pd atoms (Pd_1), Pd dimers (Pd_2) and Pd trimers in Au (Pd_3). The reaction pathway starts from the bare surface alloy initial state (noted IS in the free energy profile (Figure 5a) and the enthalpy profile (Figure 5b)), proceeds first through a molecular adsorption state of H_2 on top of a Pd atom (noted H_2), and progresses to H-H dissociation though a transition state TS-Dis to reach a structure with two adsorbed H atoms interacting with the same Pd_1 or Pd_3 ensemble (noted 2H). Calculations showed that dissociative adsorption of another D_2 molecule on a given site (Pd_1 or Pd_3) is not favored (Table S1), so that the experimentally observed HD exchange must involve H migration between two Pd ensembles over Au. Indeed, from the 2H intermediate, one H atom can migrate through a transition state (TS-M) to the Au surface forming H(Pd,Au). D_2 will react similarly on another surface Pd ensemble site; D will migrate to an H-containing site to place H and D atoms on the same site. Atom recombination to yield HD, H_2 or D_2would occur through the reverse pathways shown in Figure 5a and 5b.

The nature of the Pd ensemble (Pd_1 or Pd_3) has a major impact on stability of the dissociated intermediate: the 2H state is ~0.5 eV more stable for Pd_3 compared to Pd_1, meaning that hydrogen is more strongly bound on Pd_3 than on Pd_1. This has a crucial influence of the nature of the rate controlling intermediate and transition state. Since the H atom is only weakly stabilized on Pd_1, the initial H_2 dissociation occurs with a rather high free energy for the transition state (+ 0.64 eV), as the loss of H_2 entropy in the gas phase

is not compensated by the (weak) interaction energy with Pd_1. As a result, the highest free energy difference along the pathway is between the bare surface with gas phase H_2 (IS) and the TS for H_2 dissociation (TS-Dis) (Figure 5a, energy span=0.64 eV).[28] In contrast for Pd_3, where H interacts more strongly, the 2H intermediate becomes the lowest point on the free energy surface, and the free energy span is moved to the recombination direction, occurring between 2H and the adsorbed H_2 molecular state (Figure 5a, energy span=0.39 eV). Notably, bulk Pd and Pd trimers have the same rate controlling step, indicating that there will not be qualitative differences for Pd ensembles with more than 3 atoms.

From the energetic span theory of reaction kinetics,[28] the reaction TOF can be approximated as $kT/h \exp(-\Delta G_{span}/kT)$, showing that the Pd_3 site is clearly more active than the Pd_1 one, which is in line with the experimentally obtained TOFs (Figure 4). The transition states or intermediate states for H migration onto Au are not involved in the determination of the energetic span for either the Pd_1 or Pd_3 ensembles, meaning that migration onto gold is not rate limiting in the HD exchange process. The different rate limiting intermediate for Pd_1 and Pd_3 ensembles also has strong influence on the effective enthalpy barriers, which must be evaluated between the same extreme structures as the energy span (Figure 5). Pd_1 shows an effective enthalpy barrier of 0.15 eV, much smaller than that of Pd_3 (0.5 eV), indicating that the larger rate for Pd_3 is of entropic origin.

Discussion

The combination of experimental and theoretical findings suggests that the increase in HD exchange TOF and in apparent activation energy from Pd_4Au_{96} to Pd_8Au_{92} is related to an increase in Pd ensemble size at the nanoparticle surface as the total Pd content increases. Theory and experiment are in good qualitative agreement. A key conclusion is that the difference in reactivity is of entropic origin and not based on the enthalpy profile and that this is due to a change in the TOF-limiting process when changing the ensemble size. Pd_1 (and more generally very small ensembles) stabilize adsorbed atomic H only rather weakly and show the hydrogen dissociation from gas phase H_2 as TOF-limiting, a process associated with a large entropy loss for the H_2 molecule. Pd_3 (and more generally large ensembles) stabilize more strongly adsorbed H, and the TOF-limiting process switches to the recombination of 2H adsorbed to form H_2 adsorbed on the catalyst, a process that involves only adsorbed species and is hence associated with a very small change in entropy.

Such a change in the nature of the active site (e.g. from single Pd atoms to larger Pd ensembles, e.g. trimers) and in the apparent activation entropy is supported by our experimental data. The increase in

catalytic activity from Pd_4Au_{96} to Pd_8Au_{92} does not appear to result from a simple increase in the number of the same type of active sites. Rather, the apparent activation energies are distinctly different, and the pre-exponential factor increased by a factor $6 \cdot 10^5$, not by a factor 2 when increasing the Pd content from 4 to 8 atm% Pd. This strongly suggests that the increase in pre-exponential factor is due to a change in apparent activation entropy, and unlikely due to a large increase in active sites. DFT calculations indicate that both the change in apparent activation energy and pre-exponential factor originate from a change in the rate limiting process. For single atoms, dissociation from gas phase H_2 to chemisorbed H atoms is rate limiting. On larger Pd ensembles, just as on pure Pd,[27] recombination of chemisorbed H atoms to chemisorbed H_2 is rate limiting due to the stronger hydrogen-Pd ensemble bond compared to the hydrogen-single Pd atom bond.[12,14] Similarly, the binding energies of carbon mono-oxide[29,30] and oxygen[14] have been reported to increase with increasing Pd ensemble size for Au-Pd single crystal surfaces.

There are some quantitative differences between experiment and theory in the apparent activation energy values. However, the difference in the activation energies from experiment and theory are below 0.2 eV, which is the general accuracy of the DFT exchange correlation functionals. Approximation in the simplified energetic span model used here, with no differentiation between H_2, D_2 and HD, versus a detailed microkinetic simulation could also play a role. Furthermore, the model for the catalytic surface is simplified with only one type of Pd ensemble, while the experimental surface should contain a distribution of Pd ensembles, depending on the composition and pretreatment, and also defects as steps.

Detailed determination of the ensemble sizes present in dilute alloys under reaction conditions remains a significant challenge. Thus, the ensemble sizes in the PdAu NPs in the RCT SiO_2 framework are not known under reaction conditions. It is reasonable to expect that, after the pretreatment under O_2, there will be a distribution of Pd atoms, including some single atoms, dimers and trimers. Previous CO-DRIFTS experiments showed that Pd single atoms predominated for Pd_2Au_{98} and that there were also larger Pd ensembles present for Pd_9Au_{91} RCT SiO_2.[19] However, these experiments were not performed under reaction conditions and CO is known to change the distribution of Pd on alloy surfaces.[8,31] Quantitative scanning tunneling microscopy on Au-Pd single crystals by Takehiro *et al.*[13] showed that single Pd atoms predominate in the dilute limit (~3.5 atm% Pd) and that Pd dimers and trimers are formed upon increasing the Pd surface concentration to 12.5 atm%. Larger ensembles were only observed above 20% Pd. Nevertheless, the ensemble size in the catalyst materials investigated under reaction conditions remains open; in particular, because pretreatment in O_2 at high temperature is expected to induce Pd segregation and Pd aggregation at the surface.[24] Despite this uncertainty in Pd ensemble sizes under reaction

conditions, it is reasonable based on the alignment between theory and experiment to assume an increase in Pd ensemble size when increasing the Pd concentration from 4 to 8 atm%.

No obvious indications for hydrogen dissolution into the subsurface of the dilute alloy nanoparticles were found for the alloy catalysts, whereas hydride formation does occur in the monometallic Pd catalyst (Figure S4). In the latter case, clear hysteresis between the heating and cooling curve was observed, combined with an increase in pre-exponential factor upon cooling, which was not observed for the Pd_4Au_{96} and Pd_8Au_{92} RCT SiO_2 catalysts (Figure 2, Figure 3). The slight hysteresis for Pd_8Au_{92} is attributed to changes in the Pd ensemble size; however, formation of a Pd hydride cannot be completely ruled out. Formation of Pd hydride would require three dimensional Pd islands and is therefore deemed unlikely. Indeed, previous work shows that hydride formation in PdAu alloy nanoparticle requires relatively high Pd concentrations (≥25 atm% Pd) and large Pd ensembles in Au.[15,32] Hydride formation generally leads to over-hydrogenation and a poor selectivity in alkyne and alkene hydrogenation.[33] Hence, dilute alloy catalysts are an effective design in preventing the formation of subsurface hydrogen without compromising the hydrogen dissociation activity.

Finally, our results indicated that migration between the Pd sites via Au likely occurred. DFT calculations suggested only one H_2 or D_2 molecule can adsorb on Pd_1, Pd_2 and Pd_3 ensemble in Au (Table S1). Scrambling of H and D as observed experimentally implies migration between Pd ensembles, but, as shown by calculations, is not rate determining. Surface science work on single crystal dilute Pd in Au alloys at low temperature (100-350 K) indeed provides evidence for such migration processes, although in certain cases molecules such as CO[10] and hexyne,[5] which strongly bind to Pd_1, were needed to drive hydrogen migration from the single Pd atoms onto Au. The observed scrambling in our experiments is in part due the higher temperature and H_2/D_2 pressure used.[15] Both dissociation and recombination occur on the Pd sites and not on Au, since dissociation on Au sites is calculated to be endothermic (positive ΔH) with a high barrier,[34] in line with the very low catalytic activity of the monometallic Au catalysts, the thermodynamic instability of H atoms on Au,[10] and with previously reported desorption studies.[5,12] Furthermore, recombination on gold could not explain the observed increase in apparent activation energy from Pd_4Au_{96} to Pd_8Au_{92}.

Conclusions

Our combined experimental and theory study addresses the kinetics and energetics of hydrogen dissociation, migration and recombination on real nanoparticle catalysts operating at catalytically relevant pressures and temperatures, which to the best of our knowledge has not been achieved before. Our results show that the kinetics of HD exchange on dilute Pd-in-Au catalysts are controlled by the size of surface Pd ensembles. Experimentally, the HD exchange rate and apparent activation enthalpy increased when increasing the bulk Pd content from 4% to 8%. The calculated free energy and enthalpy profiles show that this change in catalytic behavior can be ascribed to an increase in Pd ensemble size, leading to a change in the rate limiting process from dissociation of gas phase H_2 on Pd_1 (with a marked entropy change), to the recombination of adsorbed H on Pd_3 (with little entropy change), and an increase in activation enthalpy. Experiment and calculations concur in showing that the enhanced rate at larger Pd concentration or ensemble size is due to entropic effects, with a strong increase of the pre-exponential factor, but a decrease in the exponential enthalpic term. Dissolution of hydrogen into the subsurface did not occur in the dilute alloy catalysts, in contrast to monometallic Pd, a key factor for preventing over-hydrogenation in selective hydrogenation catalysis. Altogether, this study shows that the rate-controlling step for a catalytic mechanism can be tuned by the formation of specific metastable ensembles at the surface of the alloy, that are maintained during reaction at moderate temperature, opening promises for the rational control of hydrogenation reactions through optimal active ensembles.

Methods

Chemicals

All chemicals were used as received without further purification. Hydrogen tetrachloroaurate trihydrate ($HAuCl_4 \cdot 3H_2O$, ≥99.9%), sodium borohydride ($NaBH_4$, 99 %), sodium tetrachloropalladate (Na_2PdCl_4, ≥99.99%), sodium citrate tribasic dihydrate (≥99.0%), potassium carbonate (K_2CO_3, ≥99.0%), tannic acid, L-ascorbic acid (≥99.0 %) polyvinylpyrrolidone (PVP, M_w ~55000 g/mol), styrene (contains 4-tert-butylcatechol as stabilizer, ≥99%), 2,2'-Azobis(2-methylpropionamidine) dihydrochloride (AAPH, 97%), tetraethyl orthosilicate (TEOS, 98%) were purchased from Sigma-Aldrich. Absolute ethanol (EtOH) was purchased from KOPTEC. Ultrapure water (Millipore Milli-Q grade) with a resistivity of 18.2 MΩ was used in all of the experiments. All glassware for the AuNP synthesis was cleaned with fresh aqua regia (HCl/HNO_3 in a 3:1 volume ratio), rinsed with large amounts of water and dried at 403 K before usage.

Catalyst synthesis

Gold nanoparticles: the procedure described by Piella *et al.* was followed to synthesize monodisperse gold nanoparticles.[35] Briefly, 450 mL 2.2 mM trisodium citrate in MilliQ water was added to a aqua regia clean 1L two-neck round bottom flask connected to a (ice-)water cooled reflux condenser. The reaction mixture was heated to 343 K in an oil bath, while stirring magnetically at 400 rpm (revolutions per minute). Next, 0.3 mL 2.5 mM tannic acid and 3.0 mL 150 mM K_2CO_3 were added while increasing the stirring speed to 700 rpm. Thereafter, 3.0 mL 25 mM $HAuCl_4$ in H_2O were added. The reaction mixture instantaneously turned from yellow to gray, and a few minutes later to orange-red. After 10 minutes, 165 mL of the reaction mixture was removed, and 165 mL 2.2 mM sodium citrate solution was added. Next, 1.5 mL 25 mM $HAuCl_4$ solution were added. After10 min, the reaction mixture was cooled down from 343 K to room temperature.

Raspberry colloids: the raspberry colloids were prepared by attaching the gold nanoparticles to the sacrificial polystyrene colloids (d_{PS} = 393 nm). To 150 mL AuNPs, 1.5 mL aqueous PVP solution (0.1 g PVP per mL H_2O) was added. Subsequently, the NP dispersion was added to 12 mL thiol-functionalized PS colloids (5.0 wt% in water) in a drop-wise fashion under continuous stirring at 400 rpm. Next, the raspberry colloids were washed 3 times with MQ H_2O (centrifugation: 14000 g x 30 min) and re-dispersed in 12 mL MQ H_2O (5.0 wt% PS in water).

Pd overgrowth: the Pd growth on the AuNPs attached to polystyrene colloids was performed at low pH to ensure sufficiently slow reaction rates and selective growth on the AuNPs.[36] 12 mL raspberry colloid dispersion (5.0 wt% PS in water) were diluted to 150 mL in MQ H_2O. Next, 1.5 mL 0.1 M HCl was added to

lower the pH to ~4, while stirring the reaction mixture at 400 rpm. Next, 120 µL 10 mM Na_2PdCl_4 and 120 µL 40 mM ascorbic acid were added to obtain the Pd_4Au_{96} NPs, and 270 µL 10 mM Na_2PdCl_4 and 270 µL 40 mM ascorbic acid were added to obtain the Pd_8Au_{92} NPs. The mixture was left to react for 1h. Next, the raspberry colloids were washed twice with 150 mL MQ H_2O at 12000 g for 30 min and finally redispersed in 12 mL MQ H_2O (5.0 wt% PS in water).

RCT preparation: 3 x 4 mL raspberry colloid dispersion (5.0 wt% PS in water) were dried in 3 separate conical vials at 65 °C in air. To each vial ~200 µL of pre-hydrolyzed TEOS solution (33 vol% of a 0.10 M HCl in H_2O solution, 33 vol% ethanol, 33 vol% TEOS) was added to infiltrate the dried colloidal crystal. Thereafter the sample was dried again at 65 °C. This step was repeated 3 times. The samples were calcined to remove PS colloids by heating them in static air from room temperature to 773 K with 1.9 K/min and held at 773 K for 2 h, and then cooled to room temperature over 3-4 h.

Structural Characterization

Electron microscopy was used for structural analysis. The samples were dispersed in absolute ethanol and drop-cased onto a Formvar/Carbon 200 mesh copper grid (TedPella). Bright field transmission electron microscopy imaging was carried out using a JEOL 2100 TEM operated at 200 kV. The High Angle Annular Dark Field-Scanning Transmission Electron Microscopy (HAADF-STEM) and Energy-dispersive X-ray spectroscopy (EDX) were performed using a JEOL ARM 200F STEM equipped with a cold field emission gun (FEG, operated at 200 keV) and integrated aberration corrector (Cs). Inductively coupled plasma mass spectrometry (ICP-MS, Agilent Technologies 7700x) was used for compositional analysis (metal composition and metal weight loading).

Catalysis experiments

Prior to catalysis the RCT catalysts were sieved (100-300 µm). Due to difference in activity between the samples the amount loaded to the reactor was adjusted to maintain nearly similar conversions for the different catalysts in the same temperature range. For the Pd_0Au_{100}, Pd_4Au_{96}, Pd_8Au_{92} and $Pd_{100}Au_0$ RCT catalysts 78, 20, 5 and 2 mg, respectively, were loaded to cylindrical quartz reactor tube with an inner diameter of 1 cm. Next, the catalysts were diluted in quartz sand to obtain a 1 cm bed height. Thereafter, the catalysts were pretreated in 20 % O_2 in Ar at a flow rate of 50 mL/min to segregate Pd to the NP surface in case of the bimetallic samples.[24] To this end, the catalysts were heated to 500 °C with 10 K/min and kept at 773 K for 30 min. Thereafter, the catalysts were cooled in 40 mL/min Ar to 373 K. From 373 K to RT the catalyst was cooled in 20% H_2 in Ar to ensure reduction of the Pd atoms. In the temperature programmed HD exchange experiments (Figure 2, Figure 3 and Figure S1), the reaction mixture was composed of 10%

H_2 and 10% D_2 in Ar, total flow rate was 50 mL/min. In the reaction order experiments (Figure S2), the H_2 and D_2 concentration in the gas mixture was varied while retaining a total flow rate of 50 mL/min. The temperature was kept constant at the temperature at which the HD conversion was 5%, which was typically between 343 and 373 K. The reaction products were analyzed using an online mass spectrometer (Hiden HAL 301/3F Series) measuring m/z=2, 3, 4 and 40 to quantify the amount of H_2, HD, D_2 and Ar, respectively. The inlet pressure for the MS was set at $9 \cdot 10^{-7}$ torr and the scan rate was typically 0.1-1 channel/s. The sensitivity of the MS for each m/z value was set between -7 and -10 depending on the concentration of each component in the reaction mixture.

Quantitative mass spectrometry analysis

Quantification of the measured mass spec intensity was carried out as follows. First, the baseline for each of the signals (m/z = 2, 3, and 4) was determined using the data recorded over the bypass before and after the reaction. Note that due to differences in the transmission cross-section, the sensitivity of the mass spec is not the same for the different isotopes, where H_2 > HD > D_2. The baselines for each of the m/z values were used to determine the sensitivity of the mass spec, expressed in intensity (# counts) per gas flow (mL/min), as a function of reaction time. In this we made use of the fact that the D_2 and H_2 flow were known and the stoichiometry in which they form HD is 1 D_2: 1 H_2:2HD. Next, the conversion and activity were calculated based on the HD signal, which had the lowest signal to noise ratio. The maximum conversion was 50% which corresponds to a statistical mixture of 1 D_2: 1 H_2:2HD. From the conversion data the corresponding activity was calculated, where the activity was expressed in the amount of HD (in micromole) converted per second per gram of metal loaded to the reactor. The activity of the isothermal steps with a conversion between 1 and 20% where then used to make the Arrhenius plot in which Ln(activity) was plotted as a function of the inverse temperature in Kelvin. Linearly fitting these data provided the apparent activation energy and pre-exponential factor.

Extracting the pre-exponential factor

The rate expression can be written as:

$$r = k_{app} \cdot \left(\frac{P_{H_2}}{P_{ref}}\right)^{n_{H_2}} \cdot \left(\frac{P_{D_2}}{P_{ref}}\right)^{n_{D_2}}$$

where r is the reaction rate in μmol_{HD} per second per gram catalyst, k_{app} is the apparent rate constant, P_{H_2} and P_{D_2} are the partial pressures of hydrogen and deuterium, n_{H_2} and n_{D_2} are the apparent rate

orders for hydrogen and deuterium, and P_{ref} is equal to 1 atm (the fugacity of an ideal gas at standard temperature and pressure).

In the scenario where the pressures of the two gases are equal this simplifies to:

$$r = k_{app} \cdot \left(P_{H_2}\right)^{n_{H_2}+n_{D_2}}$$

Expanding the rate constant into an Arrhenius form gives:

$$r = A_{app} \cdot e^{-\frac{Ea}{RT}} \cdot \left(P_{H_2}\right)^{n_{H_2}+n_{D_2}}$$

The intercept (b) of an Arrhenius plot of $\ln(r)$ versus $1/T$ is therefore:

$$b = \ln\left(A_{app}\right) + \left(n_{H_2} + n_{D_2}\right)\ln\left(P_{H_2}\right)$$

The apparent pre-exponential factor A_{app} can be obtained by rearrangement of the equation above. The value of $n_{H_2} + n_{D_2}$ was experimentally determined to be approximately 1 under the conditions examined (Figure S2). The entropic portion of the apparent pre-exponential factor can be approximated with transition state theory where:

$$A_{app} = N_{sites} \cdot \frac{k_B T}{h} \cdot e^{\frac{S_{act,app}}{R}}$$

Here N_{sites} is the number of reactive sites in µmoles per gram catalyst, k_B is the Boltzmann constant, h is Planck's constant, T is temperature (approximately the average temperature), and $S_{act,app}$ is the apparent activation entropy.

***Turn-over-frequency* calculation**

The nanoparticle volume ($V_{particle}$) and surface area ($S_{particle}$) were calculated based on their average particle diameter ($d_{particle}$) and assuming a decahedral particle shape: $V_{particle} = \frac{5}{12}\left(3 + \sqrt{5}\right)a^3$ and $S_{particle} = 5\sqrt{3}\,a^2$ where $a = \frac{d_{particle}}{2\times 0.95}$. The number of Pd and Au surface atoms was computed using their Van der Waals radius and a surface packing of 0.907 corresponding to a {111} FCC crystal facet: $\#\ Au\ surface\ atoms = \frac{S_{total}\times 0.907}{2\pi\times r_{vdW}\times X_{Au}}$ and $\#\ Pd\ surface\ atoms = \frac{S_{total}\times 0.907}{2\pi\times r_{vdW}\times X_{Pd}}$. The number of accessible metal atoms was assumed to be 15% of the total number of surface atoms.[18]

DFT calculations

Pd/Au(111) metal surfaces were modelled using a 4-layer slab and a (3x3) unit cell. The bottom 2 layers

were constrained while the upper 2 layers and adsorbates were allowed to relax until the convergence threshold of 0.01eV/Å was reached. The dDsC-dispersion-corrected PBE functional,[37,38] a plane-wave basis set with a cutoff energy of 400eV and a Monkhorst-Pack[39] generated 7x7x1 K-points grid were used for all calculations. Transition states were optimized using the dimer method.[40] Vibrational frequency calculations were carried out for all transition states to ensure that only one imaginary frequency was observed. All calculations were performed with the Vienna ab initio simulation package (VASP).[41,42] Free energy calculations (performed at T= 363.15K and P= 0.2bar) are static and include translational and rotational degrees of freedom for gas phase H_2 and vibrational degrees of freedom for all systems (gas phases and surfaces) evaluated with the harmonic approximation. Enthalpy includes zero-point energy and thermal effects.

Author contributions

CMF, RJM and PS guided the research. JvdH prepared and characterized the catalysts, advised by JA, and conducted the catalysis experiments. HTN performed the DFT calculations. AT contributed to the data analysis. NE contributed to the data interpretation. All authors participated in discussions. JvdH wrote the manuscript with contributions of all authors.

Supporting Information Available: Supporting Table with the DFT calculated hydrogen adsorption energies on Pd_1 and Pd_3 surfaces. Supporting Figures containing additional electron microscopy analysis, reaction order experiments, HD exchange rates normalized per gram metal and gram Pd, HD exchange data for $Pd_{100}Au_0$, and DFT calculations for the Pd_2 surface. This information is available free of charge on the ACS Publications website.

Acknowledgment

This work was supported as part of the Integrated Mesoscale Architectures for Sustainable Catalysis (IMASC), an Energy Frontier Research Center funded by the U.S. Department of Energy, Office of Science, Basic Energy Sciences under Award # DE-SC0012573. Electron microscopy was performed at the Center for Nanoscale Systems (CNS), a member of the National Nanotechnology Coordinated Infrastructure Network (NNCI), which is supported by the National Science Foundation under NSF ECCS award no. 1541959.

References

(1) Zhang, L.; Zhou, M.; Wang, A.; Zhang, T. Selective Hydrogenation over Supported Metal Catalysts: From Nanoparticles to Single Atoms. *Chem. Rev.* **2020**, *120* (2), 683–733. https://doi.org/10.1021/acs.chemrev.9b00230.

(2) Felix Studt, Frank Abild-Pedersen, Thomas Bligaard, Rasmus Z. Sørensen, Claus H. Christensen, J. K. N. Identification of Non-Precious Metal Alloy Catalysts for Selective Hydrogenation of Acetylene. *Science (80-.).* **2008**, *320* (June), 1320–1323. https://doi.org/10.1126/science.1156660.

(3) Louis, C.; Delannoy, L. *Selective Hydrogenation of Polyunsaturated Hydrocarbons and Unsaturated Aldehydes over Bimetallic Catalysts*, 1st ed.; Elsevier Inc., 2019; Vol. 64. https://doi.org/10.1016/bs.acat.2019.08.002.

(4) Kyriakou, G.; Boucher, M. B.; Jewell, A. D.; Lewis, E. A.; Lawton, T. J.; Baber, A. E.; Tierney, H. L.; Flytzani-Stephanopoulos, M.; Sykes, E. C. H. Isolated Metal Atom Geometries as a Strategy for Selective Heterogeneous Hydrogenations. *Science (80-.).* **2012**, *335* (6073), 1209–1212. https://doi.org/10.1126/science.1215864.

(5) Liu, J.; Uhlman, M. B.; Montemore, M. M.; Trimpalis, A.; Giannakakis, G.; Shan, J.; Cao, S.; Hannagan, R. T.; Sykes, E. C. H.; Flytzani-Stephanopoulos, M. Integrated Catalysis-Surface Science-Theory Approach to Understand Selectivity in the Hydrogenation of 1-Hexyne to 1-Hexene on PdAu Single-Atom Alloy Catalysts. *ACS Catal.* **2019**, *9* (9), 8757–8765. https://doi.org/10.1021/acscatal.9b00491.

(6) Luneau, M.; Shirman, T.; Foucher, A. C.; Duanmu, K.; Verbart, D. M. A.; Sautet, P.; Stach, E. A.; Aizenberg, J.; Madix, R. J.; Friend, C. M. Achieving High Selectivity for Alkyne Hydrogenation at High Conversions with Compositionally Optimized PdAu Nanoparticle Catalysts in Raspberry Colloid-Templated SiO2. *ACS Catal.* **2020**, *10* (1), 441–450. https://doi.org/10.1021/acscatal.9b04243.

(7) Hugon, A.; Delannoy, L.; Krafft, J. M.; Louis, C. Selectivehydrogenation of 1,3-Butadiene in the Presence of an Excess of Alkenes over Supported Bimetallic Gold-Palladium Catalysts. *J. Phys. Chem. C* **2010**, *114* (24), 10823–10835. https://doi.org/10.1021/jp100479b.

(8) Kolli, N. El; Delannoy, L.; Louis, C. Bimetallic Au-Pd Catalysts for Selective Hydrogenation of

Butadiene: Influence of the Preparation Method on Catalytic Properties. *J. Catal.* **2013**, *297*, 79–92. https://doi.org/10.1016/j.jcat.2012.09.022.

(9) Han, S.; Mullins, C. B. Catalytic Reactions on Pd-Au Bimetallic Model Catalysts. *Acc. Chem. Res.* **2021**, *54* (2), 379–387. https://doi.org/10.1021/acs.accounts.0c00642.

(10) Lucci, F. R.; Darby, M. T.; Mattera, M. F. G.; Ivimey, C. J.; Therrien, A. J.; Michaelides, A.; Stamatakis, M.; Sykes, E. C. H. Controlling Hydrogen Activation, Spillover, and Desorption with Pd-Au Single-Atom Alloys. *J. Phys. Chem. Lett.* **2016**, *7* (3), 480–485. https://doi.org/10.1021/acs.jpclett.5b02400.

(11) Vignola, E.; Steinmann, S. N.; Le Mapihan, K.; Vandegehuchte, B. D.; Curulla, D.; Sautet, P. Acetylene Adsorption on Pd-Ag Alloys: Evidence for Limited Island Formation and Strong Reverse Segregation from Monte Carlo Simulations. *J. Phys. Chem. C* **2018**, *122* (27), 15456–15463. https://doi.org/10.1021/acs.jpcc.8b04108.

(12) Yu, W. Y.; Mullen, G. M.; Mullins, C. B. Hydrogen Adsorption and Absorption with Pd-Au Bimetallic Surfaces. *J. Phys. Chem. C* **2013**, *117* (38), 19535–19543. https://doi.org/10.1021/jp406736b.

(13) Takehiro, N.; Liu, P.; Bergbreiter, A.; Nørskov, J. K.; Behm, R. J. Hydrogen Adsorption on Bimetallic PdAu(111) Surface Alloys: Minimum Adsorption Ensemble, Ligand and Ensemble Effects, and Ensemble Confinement. *Phys. Chem. Chem. Phys.* **2014**, *16* (43), 23930–23943. https://doi.org/10.1039/c4cp02589j.

(14) Han, S.; Mullins, C. B. Surface Alloy Composition Controlled O2 Activation on Pd-Au Bimetallic Model Catalysts. *ACS Catal.* **2018**, *8* (4), 3641–3649. https://doi.org/10.1021/acscatal.8b00140.

(15) O'Connor, C. R.; Duanmu, K.; Patel, D. A.; Muramoto, E.; van Spronsen, M. A.; Stacchiola, D.; Sykes, E. C.; Sautet, P.; Madix, R. J.; Friend, C. M. Facilitating Hydrogen Atom Migration via a Dense Phase on Palladium Islands to a Surrounding Silver Surface. *Proc. Natl. Acad. Sci. U. S. A.* **2020**, *117* (37), 22657–22664. https://doi.org/10.1073/pnas.2010413117.

(16) Tierney, H. L.; Baber, A. E.; Kitchin, J. R.; Sykes, E. C. H. Hydrogen Dissociation and Spillover on Individual Isolated Palladium Atoms. *Phys. Rev. Lett.* **2009**, *103* (24), 1–4. https://doi.org/10.1103/PhysRevLett.103.246102.

(17) Shirman, E.; Shirman, T.; Shneidman, A. V.; Grinthal, A.; Phillips, K. R.; Whelan, H.; Bulger, E.; Abramovitch, M.; Patil, J.; Nevarez, R.; Aizenberg, J. Modular Design of Advanced Catalytic

Materials Using Hybrid Organic–Inorganic Raspberry Particles. *Adv. Funct. Mater.* **2018**, *28* (27), 1–20. https://doi.org/10.1002/adfm.201704559.

(18) van der Hoeven, J. E. S.; Kraemer, S.; Dussi, S.; Shirman, T.; Rycroft, C. H.; Bell, D. C.; Friend, C. M.; Aizenberg, J. 3D Characterization of Metal-Support Interfaces in Supported Catalysts. **2021**, *submitted*.

(19) Luneau, M.; Shirman, T.; Filie, A.; Timoshenko, J.; Chen, W.; Trimpalis, A.; Flytzani-Stephanopoulos, M.; Kaxiras, E.; Frenkel, A. I.; Aizenberg, J.; Friend, C. M.; Madix, R. J. Dilute Pd/Au Alloy Nanoparticles Embedded in Colloid-Templated Porous SiO2: Stable Au-Based Oxidation Catalysts. *Chem. Mater.* **2019**, *31* (15), 5759–5768. https://doi.org/10.1021/acs.chemmater.9b01779.

(20) Shirman, T.; Toops, T. J.; Shirman, E.; Shneidman, A. V.; Liu, S.; Gurkin, K.; Alvarenga, J.; Lewandowski, M. P.; Aizenberg, M.; Aizenberg, J. Raspberry Colloid-Templated Approach for the Synthesis of Palladium-Based Oxidation Catalysts with Enhanced Hydrothermal Stability and Low-Temperature Activity. *Catal. Today* **2021**, *360* (March), 241–251. https://doi.org/10.1016/j.cattod.2020.03.037.

(21) Liu, M.; Guyot-Sionnest, P. Mechanism of Silver(I)-Assisted Growth of Gold Nanorods and Bipyramids. *J. Phys. Chem. B* **2005**, *109* (47), 22192–22200. https://doi.org/10.1021/jp054808n.

(22) Scott, M. C.; Chen, C. C.; Mecklenburg, M.; Zhu, C.; Xu, R.; Ercius, P.; Dahmen, U.; Regan, B. C.; Miao, J. Electron Tomography at 2.4-Ångström Resolution. *Nature* **2012**, *483* (7390), 444–447. https://doi.org/10.1038/nature10934.

(23) Barnard, A. S.; Young, N. P.; Kirkland, A. I.; Van Huis, M. A.; Xu, H. Nanogold: A Quantitative Phase Map. *ACS Nano* **2009**, *3* (6), 1431–1436. https://doi.org/10.1021/nn900220k.

(24) Luneau, M.; Guan, E.; Chen, W.; Foucher, A. C.; Marcella, N.; Shirman, T.; Verbart, D. M. A.; Aizenberg, J.; Aizenberg, M.; Stach, E. A.; Madix, R. J.; Frenkel, A. I.; Friend, C. M. Enhancing Catalytic Performance of Dilute Metal Alloy Nanomaterials. *Commun. Chem.* **2020**, *3* (1), 1–9. https://doi.org/10.1038/s42004-020-0293-2.

(25) Silva, T. A. G.; Ferraz, C. P.; Gonçalves, R. V.; Teixeira-Neto, E.; Wojcieszak, R.; Rossi, L. M. Restructuring of Gold-Palladium Alloyed Nanoparticles: A Step towards More Active Catalysts for Oxidation of Alcohols. *ChemCatChem* **2019**, *11* (16), 4021–4027.

https://doi.org/10.1002/cctc.201900553.

(26) Bugaev, A. L.; Guda, A. A.; Lomachenko, K. A.; Srabionyan, V. V.; Bugaev, L. A.; Soldatov, A. V.; Lamberti, C.; Dmitriev, V. P.; Van Bokhoven, J. A. Temperature- and Pressure-Dependent Hydrogen Concentration in Supported PdHx Nanoparticles by Pd K-Edge X-Ray Absorption Spectroscopy. *J. Phys. Chem. C* **2014**, *118* (19), 10416–10423. https://doi.org/10.1021/jp500734p.

(27) OBrien, C. P.; Miller, J. B.; Morreale, B. D.; Gellman, A. J. The Kinetics of H 2-D 2 Exchange over Pd, Cu, and PdCu Surfaces. *J. Phys. Chem. C* **2011**, *115* (49), 24221–24230. https://doi.org/10.1021/jp2076885.

(28) Kozuch, S.; Shaik, S. How to Conceptualize Catalytic Cycles? The Energetic Span Model. *Acc. Chem. Res.* **2011**, *44* (2), 101–110. https://doi.org/10.1021/ar1000956.

(29) Ruff, M.; Takehiro, N.; Liu, P.; Nørskov, J. K.; Behm, R. J. Size-Specific Chemistry on Bimetallic Surfaces: A Combined Experimental and Theoretical Study. *ChemPhysChem* **2007**, *8* (14), 2068–2071. https://doi.org/10.1002/cphc.200700070.

(30) Ouyang, M.; Papanikolaou, K. G.; Boubnov, A.; Hoffman, A. S.; Giannakakis, G.; Bare, S. R.; Stamatakis, M.; Flytzani-stephanopoulos, M.; Sykes, E. C. H. Alloy Catalysts. *Nat. Commun.* No. 2021, 1–11. https://doi.org/10.1038/s41467-021-21555-z.

(31) Kim, H. Y.; Henkelman, G. CO Adsorption-Driven Surface Segregation of Pd on Au/Pd Bimetallic Surfaces: Role of Defects and Effect on CO Oxidation. *ACS Catal.* **2013**, *3* (11), 2541–2546. https://doi.org/10.1021/cs4006259.

(32) Guan, E.; Foucher, A. C.; Marcella, N.; Shirman, T.; Luneau, M.; Head, A. R.; Verbart, D. M. A.; Aizenberg, J.; Friend, C. M.; Stacchiola, D.; Stach, E. A.; Frenkel, A. I. New Role of Pd Hydride as a Sensor of Surface Pd Distributions in Pd−Au Catalysts. *ChemCatChem* **2020**, *12* (3), 717–721. https://doi.org/10.1002/cctc.201901847.

(33) Teschner, D.; Borsodi, J.; Wootsch, A.; Révay, Z.; Hävecker, M.; Knop-Gericke, A.; Jackson, S. D.; Schlögl, R. The Roles of Subsurface Carbon and Hydrogen in Palladium-Catalyzed Alkyne Hydrogenation. *Science (80-.).* **2008**, *320* (5872), 86–89. https://doi.org/10.1126/science.1155200.

(34) Hammer, B.; Nørskov, J. K. Theoretical Surface Science and Catalysis—Calculations and Concepts. *Adv. Catal.* **2000**, *45* (C), 71–129. https://doi.org/10.1016/S0360-0564(02)45013-4.

(35) Piella, J.; Bastús, N. G.; Puntes, V. Size-Controlled Synthesis of Sub-10-Nanometer Citrate-Stabilized Gold Nanoparticles and Related Optical Properties. *Chem. Mater.* **2016**, *28* (4), 1066–1075. https://doi.org/10.1021/acs.chemmater.5b04406.

(36) Hoeven, J. E. S. Van Der; Deng, T.; Albrecht, W.; Olthof, L. A.; Huis, M. A. Van; Jongh, P. E. De; Blaaderen, A. Van. Structural Control over Bimetallic Core − Shell Nanorods for Surface Enhanced Raman Spectroscopy. *ACS Omega* **2021**, *6* (10), 7034–7046. https://doi.org/10.1021/acsomega.0c06321.

(37) Steinmann, S. N.; Corminboeuf, C. Comprehensive Benchmarking of a Density-Dependent Dispersion Correction. *J. Chem. Theory Comput.* **2011**, *7* (11), 3567–3577. https://doi.org/10.1021/ct200602x.

(38) Perdew, J. P.; Burke, K.; Ernzerhof, M. Generalized Gradient Approximation Made Simple. *Phys. Rev. Lett.* **1996**, *77* (18), 3865–3868. https://doi.org/10.1103/PhysRevLett.77.3865.

(39) Monkhorst, H. J.; Pack, J. D. Special Points for Brillouin-Zone Integrations. *Phys. Rev. B* **1976**, *13* (12), 5188–5192.

(40) Henkelman, G.; Jónsson, H. A Dimer Method for Finding Saddle Points on High Dimensional Potential Surfaces Using Only First Derivatives. *J. Chem. Phys.* **1999**, *111* (15), 7010–7022. https://doi.org/10.1063/1.480097.

(41) Kresse, G.; Hafner, J. Ab Initio Molecular Dynamics for Liquid Metals. *Phys. Rev. B* **1993**, *47* (1), 558–561. https://doi.org/10.1103/PhysRevB.47.558.

(42) Kresse, G.; Hafner, J. Ab Initio Molecular-Dynamics Simulation of the Liquid-Metalamorphous-Semiconductor Transition in Germanium. *Phys. Rev. B* **1994**, *49* (20), 14251–14269. https://doi.org/10.1103/PhysRevB.49.14251.

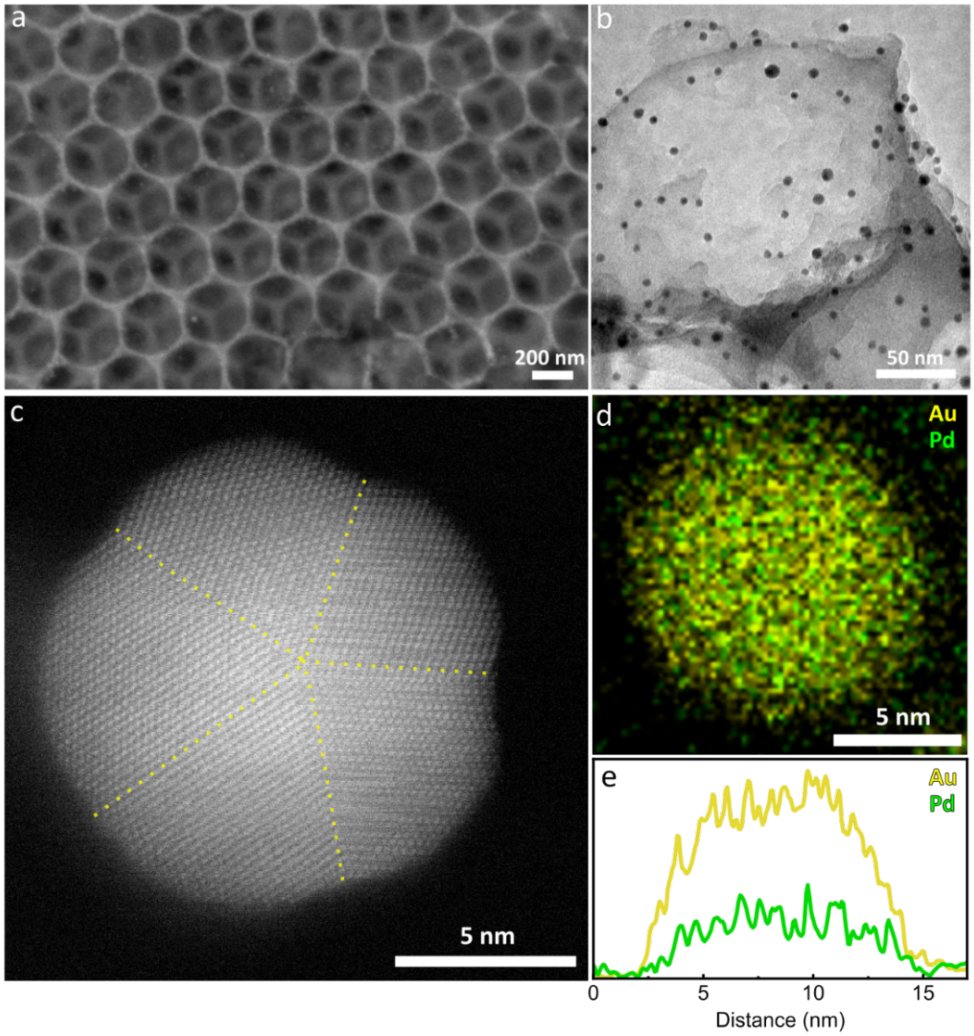

Figure 1 - Raspberry colloid templated (RCT) bimetallic Pd_4Au_{96} catalysts. a) Secondary electron microscopy (SEM) image showing the ordered macroporous silica framework. b) bright field transmission electron microscopy (BF-TEM) image of the Pd_4Au_{96} nanoparticles embedded in the silica pore walls. Size distributions can be found in Table S1 . c) High resolution high angular dark field scanning transmission electron microscopy (HAADF-STEM) image revealing the penta-twinned crystal structure of the NPs, with {111} facets exposed to the surface. d) Energy Dispersive X-ray Spectroscopy (EDX) intensity map and e) corresponding line scan along the particle diameter showing that Au and Pd in yellow and green, respectively, are well mixed throughout the particle after pretreatment.

Table 1 - **Sample details of the Pd_4Au_{96}, Pd_8Au_{92}, $Pd_{100}Au_0$ and Pd_0Au_{100} RCTs catalysts**. The average particle diameter and corresponding standard deviation were obtained from TEM and are the average of 250 size measurements per sample. The metal composition and total metal weight loading were determined from ICP-MS.

Sample ID	Diameter (nm)	Pd content (atm %)	Metal loading (wt %)	Loaded to reactor (mg)
Pd_4Au_{96}	4.9±0.9	3.6	4.2	20
Pd_8Au_{92}	5.6±0.7	7.8	4.0	5
$Pd_{100}Au_0$	6.9±1.8	100	0.59	2
Pd_0Au_{100}	6.9±2.1	0	3.3	78

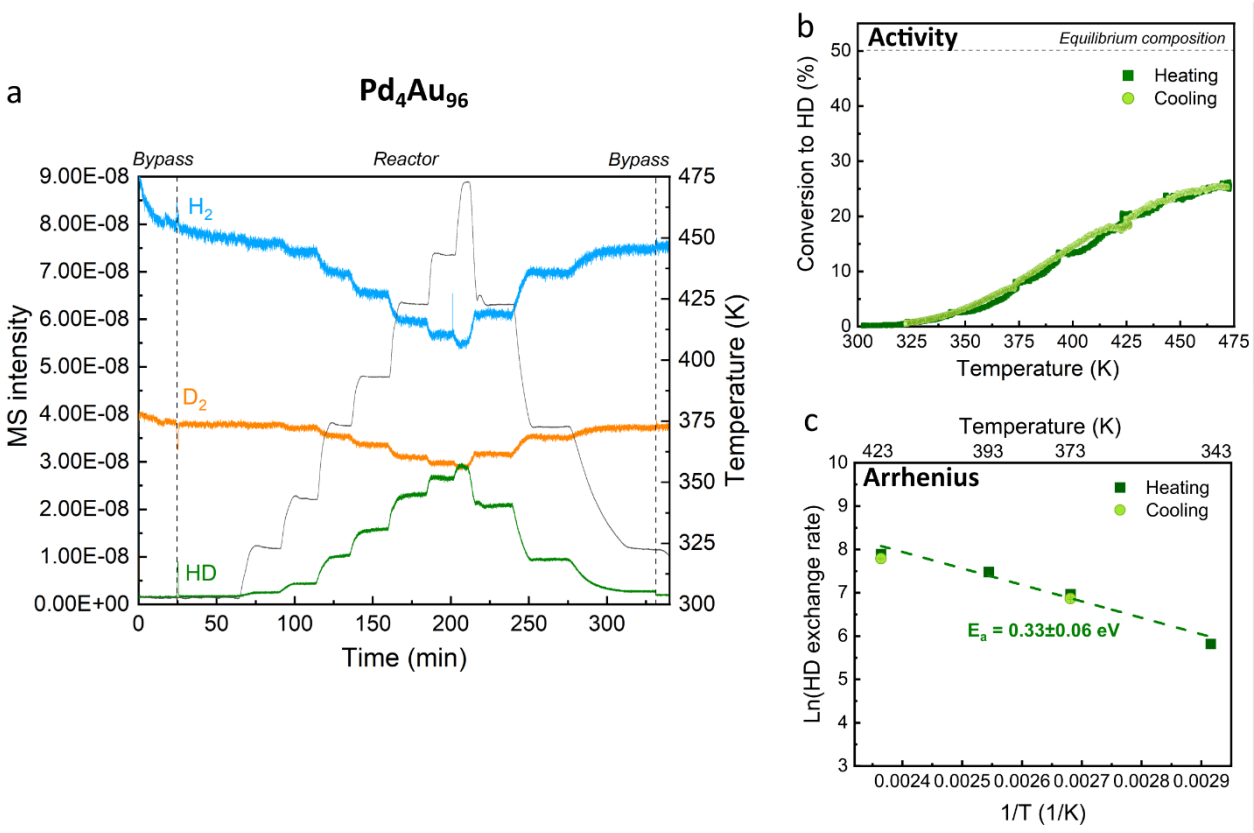

Figure 2 - HD exchange activity of the Pd_4Au_{96} RCT catalyst as a function of temperature. a) Mass spectrometry data showing the intensity (left y-axis) for H_2 (m/z=2, blue), HD (m/z=3, green) and D_2 (m/z=4, orange) as a function of time. The grey line shows the temperature profile (right y-axis). The first and last 25 min were recorded over the bypass. b) Conversion versus temperature plots during heating (dark green symbols) and cooling (light green symbols). c) Corresponding Arrhenius plot showing the data from the isothermal steps between 1 and 20% conversion. The HD exchange rate is expressed in $\mu mol_{HD}\ s^{-1}\ g_{metal}^{-1}$. The apparent activation energies and intercept during heating and cooling were 0.33±0.04 eV (32±3.8 kJ/mole) and $Ln(HD\ exchange\ rate)_{\frac{1}{T}=0}$ = 17±1.2, respectively. The data shown in b and c are based on the HD signal, which had the highest signal to noise ratio (see Methods for details on the quantification). Reaction conditions: 50 mL/min total flow containing 10% H_2 and 10% D_2 in Ar, 20 mg 4.2 wt% Pd_4Au_{96} RCT SiO_2 catalyst loaded.

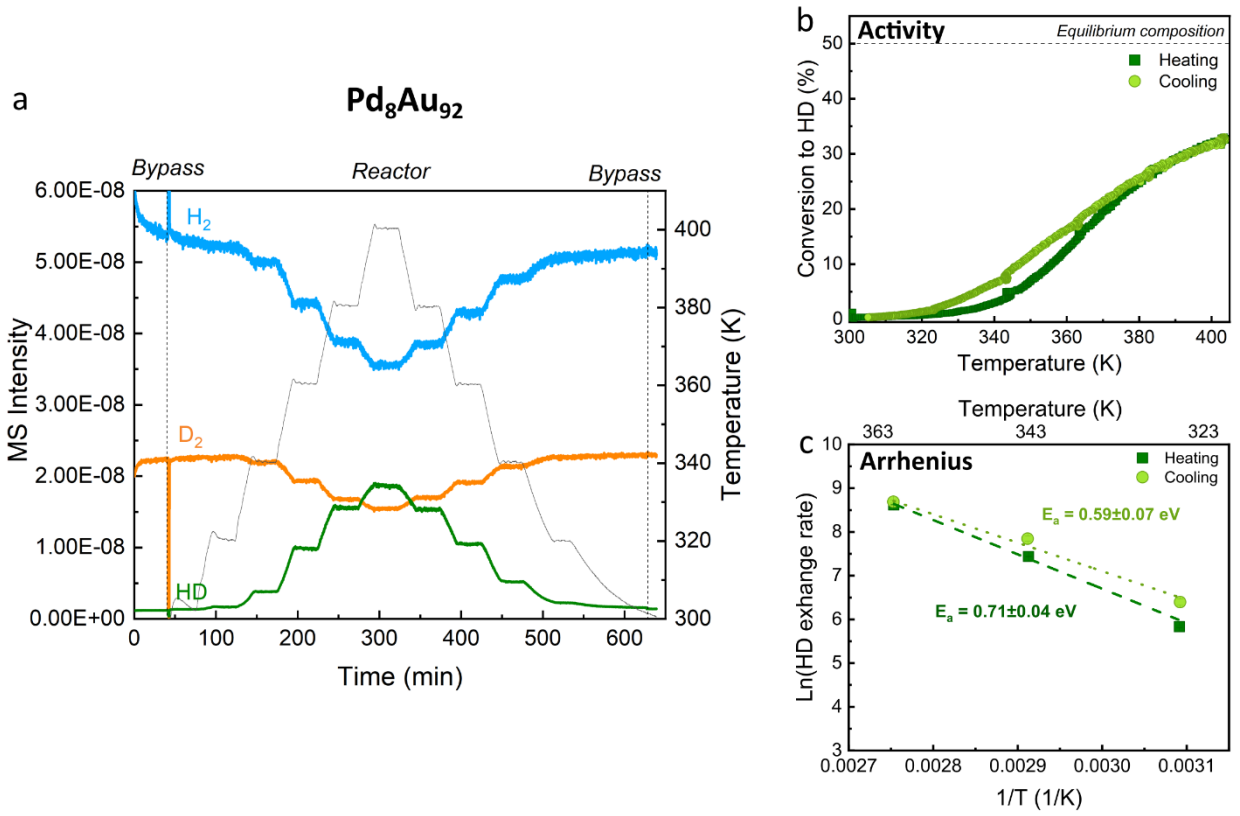

Figure 3 - HD exchange activity of the Pd_8Au_{92} RCT catalyst as a function of temperature. a) Mass spectrometry data showing the intensity (left y-axis) for H_2 (m/z=2, blue), HD (m/z=3, green) and D_2 (m/z=4, orange) as a function of time. The grey line shows the temperature profile (right y-axis). The first and last 25 min were recorded over the bypass. b) Conversion versus temperature plots during heating (dark green symbols) and cooling (light green symbols) based on the HD signal. c) Corresponding Arrhenius plot showing the data from the isothermal steps between 1 and 20% conversion. The HD exchange rate is expressed in $\mu mol_{HD}\ s^{-1}\ g_{metal}^{-1}$. The apparent activation energies and intercept during heating were 69±3.7 kJ/mole (0.71±0.04 eV) and $Ln(HD\ exchange\ rate)_{\frac{1}{T}=0}$ = 30±1.5, respectively, and during cooling 57±6.4 kJ/mole (0.59±0.07 eV) and $Ln(HD\ exchange\ rate)_{\frac{1}{T}=0}$ = 27±1.9. The data shown in b and c are based on the HD signal, which had the highest signal to noise ratio (see Methods for details on the quantification). Reaction conditions: 50 mL/min total flow containing 10% H_2 and 10% D_2 in Ar, 5.0 mg 4.0 wt% Pd_8Au_{92} RCT SiO_2 catalyst loaded.

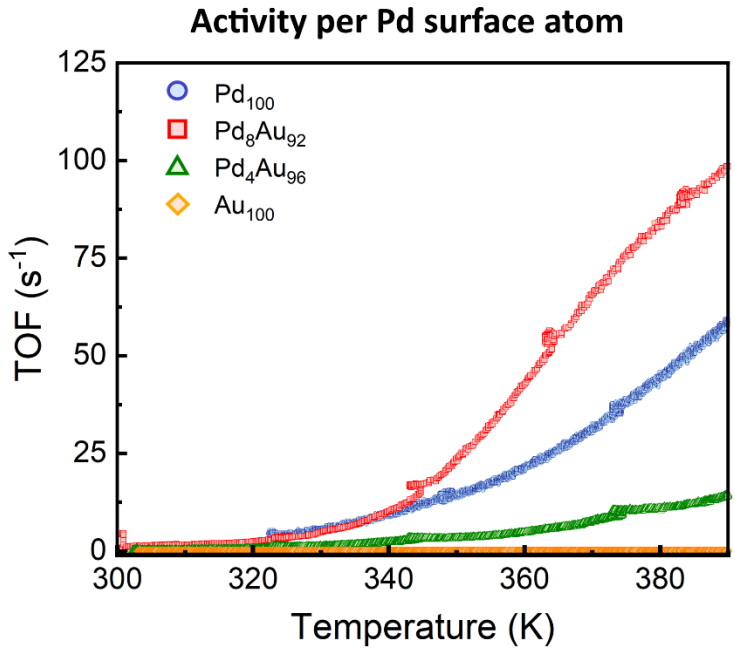

Figure 4 – Turn over frequency of $Pd_{100}Au_0$, Pd_8Au_{92}, Pd_4Au_{96} and Pd_0Au_{100} as a function of reaction temperature. TOF for $Pd_{100}Au_0$, Pd_8Au_{92}, Pd_4Au_{96} is expressed in # HD molecules converted per Pd surface atom per second. For Au_{100} the TOF is expressed per Au surface atom. A decahedral particle shape with {111} surface facets with a metal composition equal to the bulk Au:Pd ratio was assumed.

Table 2 – Apparent activation energy, Arrhenius plot intercept and corresponding pre-exponential factor of Pd_4Au_{96}, Pd_8Au_{92}, and $Pd_{100}Au_0$ RCTs catalysts. For $Pd_{100}Au_0$ the conversion data in Figure S4b were used.

Sample ID	Apparent activation energy (eV)	$Ln(HD\ exchange\ rate)_{\frac{1}{T}=0}$	Pre-exponential factor ($\mu mol_{HD}\ s^{-1}\ g^{-1}$)
Pd_4Au_{96}	0.33±0.04	17±1.2	$2.1 \cdot 10^{8}$
Pd_8Au_{92}			
Heating	0.71±0.04	30±1.5	$1.2 \cdot 10^{14}$
Cooling	0.59±0.07	27±1.9	$3.1 \cdot 10^{12}$
$Pd_{100}Au_0$			
Heating	0.45±0.01	25±0.3	$6.6 \cdot 10^{11}$
Cooling	0.46±0.01	26±0.5	$1.8 \cdot 10^{12}$

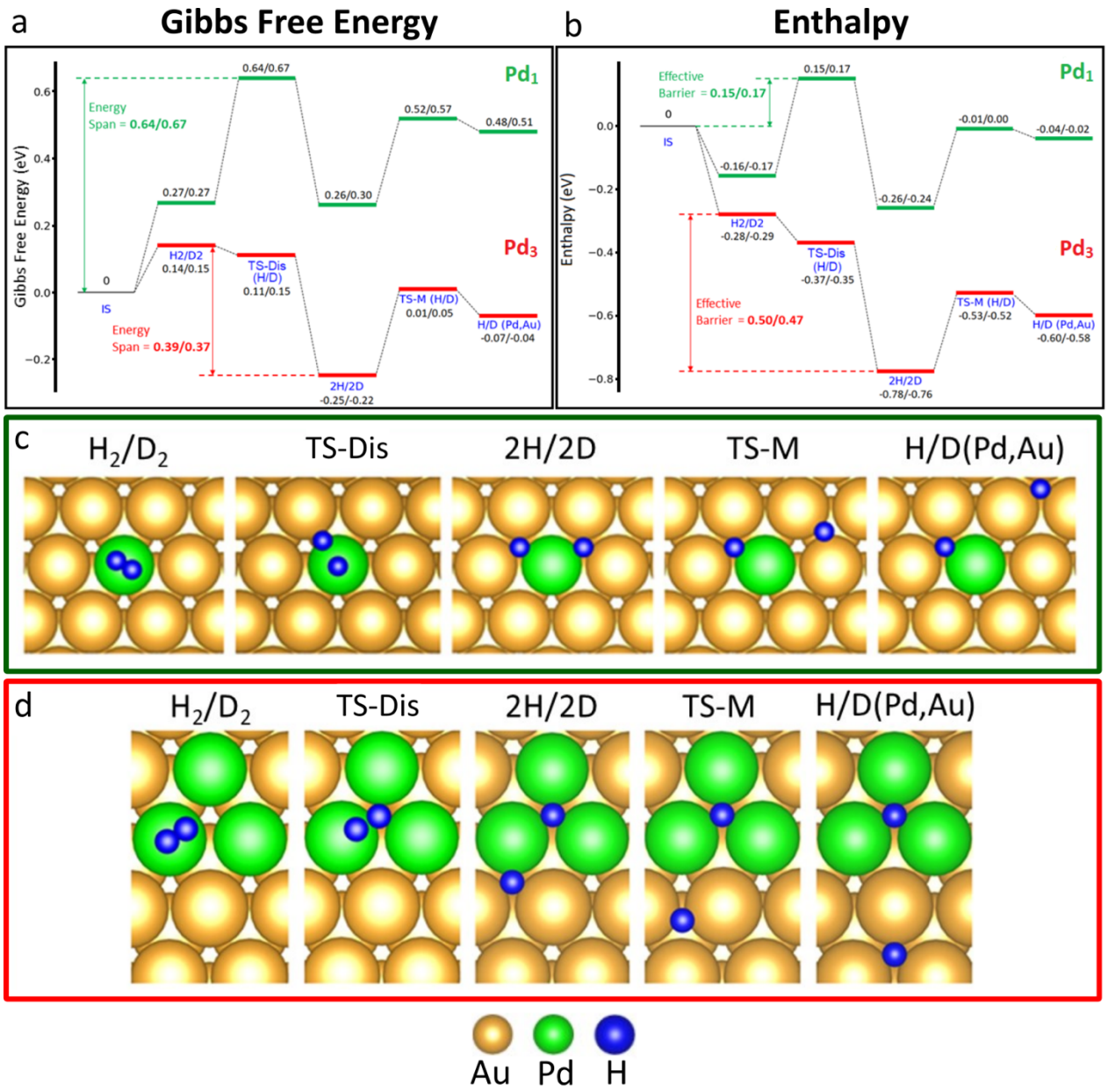

Figure 5 - Density functional theory (DFT) calculations of H_2 and D_2 adsorption, dissociation, H migration, and recombination on a Pd single atom and on a Pd trimer ensemble in a Au(111) surface. a) Gibbs free energy and b) Enthalpy profiles for Pd_1 (green) and Pd_3 (red) ensembles (in eV for T=363.15K and P=0.2bar). Free energy and enthalpy values for intermediates and transition states are provided both for H_2 (left number) and D_2 (right number) dissociation. The Gibbs free energy spans is indicated by a double end arrow: H_2/D_2 dissociation from the gas phase to the dissociation transition state for Pd_1 (0.64/0.67 eV). The reverse pathway corresponds to recombination of adsorbed H atoms to the H_2/D_2 molecular adsorption state (0.39/0.37 eV) for Pd_3. c-d) Schematics showing the different intermediates and transition states on Pd_1Au and Pd_3Au sites. From left to right: hydrogen/deuterium molecular adsorption [H_2/D_2], transition state of hydrogen/deuterium dissociation [TS-Dis], dissociated

hydrogen/deuterium in Pd containing hollow sites [2H/2D], transition state of hydrogen/deuterium migration [TS-M], and dissociated structure with one H on a pure Au hollow site [H/D (Pd,Au)].